

Stabilizing Deep Tomographic Reconstruction Networks

Weiwen Wu¹, Dianlin Hu², Shaoyu Wang³, Hengyong Yu⁴, Varut Vardhanabhuti^{1,*} and Ge Wang^{5,*}

¹Dept of Diagnostic Radiology, Queen Mary Hospital, University of Hong Kong, Hong Kong

²The Laboratory of Image Science and Technology, Southeast University, Nanjing, China

³Department of Electrical and Computer Engineering, University of Massachusetts Lowell, Lowell, MA, USA.

⁴Department of Electrical and Computer Engineering, University of Massachusetts, Lowell, MA, USA

⁵Biomedical Imaging Center, Center for Biotechnology and Interdisciplinary Studies, Department of Biomedical Engineering, School of Engineering, Rensselaer Polytechnic Institute, Troy, NY, USA

W. Wu (weiwenwu12@gmail.com); D. Hu (dianlinhu@gmail.com); S. Wang (sywang57@gmail.com); H. Yu (hengyong-yu@ieee.org); V. Vardhanabhuti (varv@hku.hk); G. Wang (wangg6@rpi.edu)

Abstract: While the field of deep tomographic reconstruction has been advancing rapidly since 2016, there are constant debates and major challenges with the recently published PNAS paper "*On instabilities of deep learning in image reconstruction and the potential costs of AI*" as a primary example, in which three kinds of instable phenomena are demonstrated: (1) tiny perturbation on input generating strong output artefacts, (2) small structural features going undetected, and (3) increased input data leading to decreased performance. In this article, we show that key algorithmic ingredients of analytic inversion, compressed sensing, iterative reconstruction, and deep learning can be synergized to stabilize deep neural networks for optimal tomographic image reconstruction. With the same or similar datasets used in the PNAS paper and relative to the same state of the art compressed sensing algorithm, our proposed analytic, compressed, iterative deep (ACID) network produces superior imaging performance that are both accurate and robust with respect to noise, under adversarial attack, and as the number of input data is increased. We believe that deep tomographic reconstruction networks can be designed to produce accurate and robust results, improve clinical and other important applications, and eventually dominate the tomographic imaging field.

Key Words: Tomographic imaging, analytic reconstruction, compressed sensing, iterative reconstruction, deep learning, image quality, stability.

I. Introduction

Tomographic imaging allows non-invasive observation and analysis of structures inside an opaque object, and has revolutionized medicine, industry and other fields. As far as medical imaging is concerned, there are 100 million computed tomography (CT) scans and 40 million magnetic resonance imaging (MRI) scans performed yearly in USA alone. In a well-known survey on medical innovations, over two-hundred leading experts scored on the relative importance of these innovations. “*The most important innovation by a considerable margin is magnetic resonance imaging (MRI) and computed tomography (CT)*”¹. Over the past several years, deep learning has attracted wide-spread attention. Since 2016, deep learning is being rapidly adapted for tomographic imaging, known as deep tomographic imaging^{2,3}. Traditionally, tomographic reconstruction algorithms are either analytic (with a closed form formulation) or iterative (based on statistical and/or compressed sensing models). Now, reconstruction algorithms can be deep neural networks, which are data-driven and learning-oriented⁴. This new type of reconstruction algorithms has generated tremendous excitement and superior results in many studies; for example, please see our recent review article for Nature Machine Intelligence⁵.

While many researchers are devoted to catch this new wave of tomographic imaging research, there are doubts and concerns on deep tomographic reconstruction as well, with the latest study⁶ as the primary example. In this study, Antun et al. performed a systematic study on instability of image reconstruction by a number of representative deep reconstruction networks including the one published in Nature⁷. This study reveals three kinds of instable phenomena: (1) tiny perturbation on input generating strong output artefacts, (2) small structural features going undetected, and (3) increased training data leading to decreased performance. These findings are both warnings and opportunities for all those who are involved in deep tomographic imaging research, development, regulation, and applications.

In a historical perspective, any debate, challenge, or crisis is the beginning of the development of new theory and methodology. In the case of tomographic imaging, there are several familiar examples. For analytic reconstruction, there was a critique that given a finite number of projections, the tomographic reconstruction is not uniquely determined (ghost structures can be reconstructed that do not show in measured data)⁸. Then, this problem was addressed by regularization such as enforcing the band-limitedness of underlying signals⁹. When iterative reconstruction algorithms were initially developed, it was observed that a reconstructed image could be strongly influenced by the penalty term; in other words, what you obtain is what you want to see by steering the solution to an under-determined inverse problem¹⁰. Then, by optimizing the regularization terms and its hyper-parameters, iterative algorithms were made into commercial scanners^{8,11}. As far as compressed sensing is concerned, there is typically a chance that a sparse solution is not correct. Theoretically speaking, the validity of compressed sensing results is under the condition of restricted isometry or robust null space property “*with an overwhelming probability*”¹² and not always accurate. For example, a tumor-like structure could be introduced, or pathological vessels might be smoothed out, if total variation is overly minimized¹³. Despite the imperfect theoretical guaranties, multiple compressed sensing reconstruction algorithms have been implemented on commercial scanners with excellent results. Indeed, as long as a method most likely delivers decent results, it would be a great tool

unless we have an even better tool.

Now, we are facing a similar situation that the emerging deep tomographic imaging methods encounter challenges in some published forms ⁶. In addition to extensive numerical and experimental data showing the instability of several deep reconstruction networks, the authors of ⁶ pointed out that these instabilities are fundamentally associated with the lack of “*kernel awareness*” ¹⁴ and “*nontrivial to overcome*” ⁶. On the other hand, compressed sensing reconstruction algorithms work much more stably in the experiments reported in ⁶, since compressed sensing algorithms are based on sparse regularization which has “*at its heart a notion of kernel awareness*” ¹⁴. In this article, we focus on demonstrating the principle that deep reconstruction networks can be stabilized to be superior to compressed sensing reconstruction alone.

Methodologically speaking, a new method does not necessarily exclude old methods, and often contain elements of old methods. For example, iterative reconstruction algorithms clearly contain key elements (projection and back-projection) of analytic reconstruction algorithms. For deep tomographic reconstruction, we have been advocating the integration of analytic, iterative, networked-based methods so that deep tomographic imaging methods would be superior to the state of the art. In Ge Wang’s presentation at NIH two years ago ¹⁵, he suggested “a superiority principle” that when we use deep learning for tomographic imaging, we can always take advantage of proven algorithms even though their results are imperfect. Then, we can train a neural network to improve upon an imperfect result effectively and efficiently. Other ways are also possible to combine classic and deep learning methods, as suggested by Wang in 2019 and shown in Fig. 1 ¹⁶.

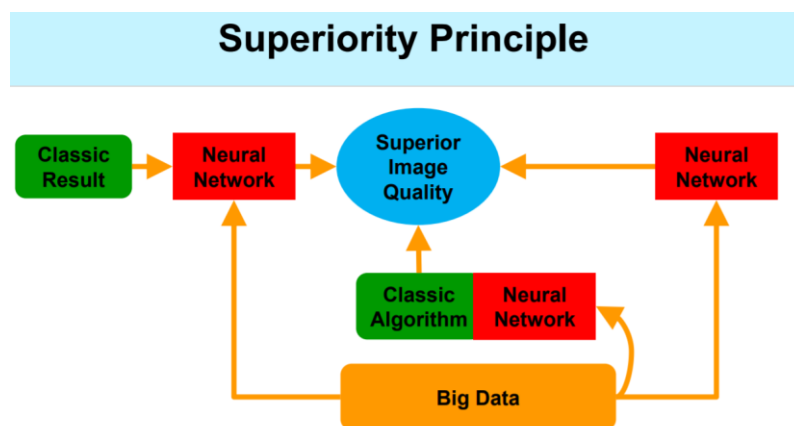


Figure 1 | Merging various types of tomographic algorithms for optimal performance.

In the scope of the study on instabilities of deep reconstruction networks ⁶, here we propose an analytic, compressive, iterative deep (ACID) network as an embodiment of the aforementioned superiority principle, and report our results to support an optimistic view that deep reconstruction algorithms can be stabilized to offer trustable results outperforming compressed sensing reconstruction. Despite resistance to or suspicion, deep tomographic reconstruction produces undeniable results, and its dominance is unavoidable in the imaging field, as evidenced by a sufficiently large number of independent studies across modalities and application areas including this study to be detailed as follows.

The rest of the paper is organized as follows. In the second section, we describe our methodology, namely, our proposed analytic, compressive, iterative deep (ACID) network. In the third section, we present our representative results showing that the ACID network produces outstanding tomographic CT and MRI reconstructions that are both accurate and stable, eliminating three kinds of instabilities reported in the PNAS paper. In the fourth section, we give our insights into the direction of which ACID is the first embodiment, discuss other relevant issues and conclude the paper.

II. Analytic, Compressive, Iterative Deep (ACID) Network

Mathematical Model: Let $\mathbf{f}^{(k)}$ be a current reconstructed image, $k=0, 1, \dots, K$, k is the index for iteration, $\mathbf{f}^{(0)}$ can be initialized to zero, \mathbf{p}_0 represents an original measurement, \mathbf{A} be an analytic transform (i.e., \mathbf{A} represents the Radon transform for CT¹⁷ and the Fourier transform for MRI¹⁸), $\Phi_w(\mathbf{p})$ a deep reconstruction network, which can transfer a tomographic dataset \mathbf{p} to a corresponding image \mathbf{f} with a vector of parameters \mathbf{w} . Let $g(\cdot)$ be a regularization term reflecting prior knowledge. The ACID mathematical model is formulated as

$$\{\mathbf{f}^{(k+1)}, \mathbf{p}^{(k+1)}\} = \arg \min_{\{\mathbf{f}, \mathbf{p}\}} \left(\frac{1}{2} \|\mathbf{f} - \mathbf{f}^{(k)} - \Phi_w(\mathbf{p})\|_F^2 + \eta g(\mathbf{f}, \mathbf{f}^{(k)}) \right), \quad \text{s.t., } \mathbf{p} = \mathbf{p}_0 - \mathbf{A}\mathbf{f}^{(k)},$$

where $\eta > 0$ is a weighting parameter. This is a constrained optimization problem and can be converted into following unconstrained counterpart:¹⁹

$$\{\mathbf{f}^{(k+1)}, \mathbf{p}^{(k+1)}\} = \arg \min_{\{\mathbf{f}, \mathbf{p}\}} \frac{1}{2} \|\mathbf{f} - \mathbf{f}^{(k)} - \Phi_w(\mathbf{p})\|_F^2 + \eta g(\mathbf{f}, \mathbf{f}^{(k)}) + \frac{\lambda}{2} \|\mathbf{p} - (\mathbf{p}_0 - \mathbf{A}\mathbf{f}^{(k)})\|_F^2,$$

It is equivalent to

$$\{\mathbf{f}^{(k+1)}, \mathbf{p}^{(k+1)}\} = \arg \min_{\{\mathbf{f}, \mathbf{p}\}} \frac{1}{2} \|\mathbf{p} - (\mathbf{p}_0 - \mathbf{A}\mathbf{f}^{(k)})\|_F^2 + \lambda \left(\frac{1}{2} \|\mathbf{f} - \mathbf{f}^{(k)} - \Phi_w(\mathbf{p})\|_F^2 + \eta g(\mathbf{f}, \mathbf{f}^{(k)}) \right),$$

where the first term can be considered as the data fidelity requirement, and the second term can be treated as the prior knowledge condition, which can be viewed as, for example, a combination of a deep image prior and a compressed sensing objective. In this initial study, we apply the sparsity over both the initially learned image and subsequent images, which can be selected in a task-specific fashion.

Since this formula demands the optimization of $\Phi_w(\mathbf{p})$, which is computationally challenging,

by replacing $\Phi_w(\mathbf{p})$ with \mathbf{u} we convert it to the following form:

$$\{\mathbf{f}^{(k+1)}, \mathbf{p}^{(k+1)}, \mathbf{u}^{(k+1)}\} = \arg \min_{\{\mathbf{f}, \mathbf{p}, \mathbf{u}\}} \frac{1}{2} \|\mathbf{p} - (\mathbf{p}_0 - \mathbf{A}\mathbf{f}^{(k)})\|_F^2 + \lambda \left(\frac{1}{2} \|\mathbf{f} - \mathbf{f}^{(k)} - \mathbf{u}\|_F^2 + \eta g(\mathbf{f}, \mathbf{f}^{(k)}) \right), \quad \text{s.t., } \mathbf{u} = \Phi_w(\mathbf{p})$$

by introducing a coupling factor $\mu > 0$ we cast it to the following unconstrained problem:

$$\{\mathbf{f}^{(k+1)}, \mathbf{p}^{(k+1)}, \mathbf{u}^{(k+1)}\} = \arg \min_{\{\mathbf{f}, \mathbf{p}, \mathbf{u}\}} \frac{1}{2} \|\mathbf{p} - (\mathbf{p}_0 - \mathbf{A}\mathbf{f}^{(k)})\|_F^2 + \lambda \left(\frac{1}{2} \|\mathbf{f} - \mathbf{f}^{(k)} - \mathbf{u}\|_F^2 + \eta g(\mathbf{f}, \mathbf{f}^{(k)}) \right) + \frac{\mu}{2} \|\mathbf{u} - \Phi_w(\mathbf{p})\|_F^2$$

where there are three variables to be optimized. Actually, it can be further divided into three sub-problems: the sub-problem of solving for \mathbf{p} , the sub-problem for \mathbf{u} and the sub-problem for \mathbf{f} , which can be respectively written as follows:

$$\mathbf{p}^{(k+1)} = \arg \min_{\mathbf{p}} \frac{1}{2} \left\| \mathbf{p} - (\mathbf{p}_0 - \mathbf{A}\mathbf{f}^{(k)}) \right\|_F^2 + \frac{\mu}{2} \left\| \mathbf{u}^{(k)} - \Phi_{\mathbf{w}}(\mathbf{p}) \right\|_F^2,$$

$$\mathbf{u}^{(k+1)} = \arg \min_{\mathbf{u}} \frac{\lambda}{2} \left\| \mathbf{f}^{(k)} - \mathbf{f}^{(k)} - \mathbf{u} \right\|_F^2 + \frac{\mu}{2} \left\| \mathbf{u} - \Phi_{\mathbf{w}}(\mathbf{p}^{(k+1)}) \right\|_F^2,$$

$$\mathbf{f}^{(k+1)} = \arg \min_{\mathbf{f}} \frac{1}{2} \left\| \mathbf{f} - \mathbf{f}^{(k)} - \mathbf{u}^{(k+1)} \right\|_F^2 + \eta g(\mathbf{f}, \mathbf{f}^{(k)}).$$

As far as the sub-problem of solving for \mathbf{p} is concerned, the solution can be given as

$$\mathbf{p}^{(k+1)} = \left(\mu \left(\frac{d(\Phi_{\mathbf{w}}(\mathbf{p}))}{d\mathbf{w}} \times \frac{d\mathbf{w}}{d\mathbf{p}} \right)^T \Bigg|_{\mathbf{p}=\mathbf{p}^{(k)}} \times (\mathbf{u}^{(k)}) + (\mathbf{p}_0 - \mathbf{A}\mathbf{f}^{(k)}) \right) / \left(\mathbf{I} + \mu \left(\frac{d(\Phi_{\mathbf{w}}(\mathbf{p}))}{d\mathbf{w}} \times \frac{d\mathbf{w}}{d\mathbf{p}} \right)^T \Bigg|_{\mathbf{p}=\mathbf{p}^{(k)}} \times \Phi_{\mathbf{w}}(\mathbf{p}^{(k)}) \right),$$

where \mathbf{I} denotes the identity transformation, $\left(\frac{d(\Phi_{\mathbf{w}}(\mathbf{p}))}{d\mathbf{w}} \times \frac{d\mathbf{w}}{d\mathbf{p}} \right)^T$ can be considered the

backpropagation of the neural network function transforming one reconstructed image to tomographic measurements, which cannot be perfectly found in practice. Actually, we can replace it with \mathbf{A} , i.e., it can be chosen as the inverse Radon transform for CT or the inverse

Fourier transform for MRI. $\left(\frac{d(\Phi_{\mathbf{w}}(\mathbf{p}))}{d\mathbf{w}} \times \frac{d\mathbf{w}}{d\mathbf{p}} \right)^T \Bigg|_{\mathbf{p}=\mathbf{p}^{(k)}} \times \Phi_{\mathbf{w}}(\mathbf{p}^{(k)})$ can be approximated by the

identity transformation \mathbf{I} . Then, $\mathbf{p}^{(k+1)}$ can be simplified as

$$\mathbf{p}^{(k+1)} = \left(\mu \mathbf{A}(\mathbf{u}^{(k)}) + (\mathbf{p}_0 - \mathbf{A}\mathbf{f}^{(k)}) \right) / (1 + \mu).$$

Regarding the sub-problem for \mathbf{u} , the solution can be directly obtained:

$$\mathbf{u}^{(k+1)} = \mu \times \Phi_{\mathbf{w}}(\mathbf{p}^{(k+1)}) / (\lambda + \mu).$$

To find the solution to the sub-problem for \mathbf{f} , we let $g(\mathbf{f}, \mathbf{f}^{(k)})$ be simplified to $g(\mathbf{f})$. In this case, the penalty will be only on image \mathbf{f} without reference to $\mathbf{f}^{(k)}$. Of course, there are many different forms of $g(\mathbf{f}, \mathbf{f}^{(k)})$ can be chosen, such as $g(\mathbf{f} - \mathbf{f}^{(k)})$ or involving all previously reconstructed intermediate images (to estimate moments etc.). Then, we can obtain the final reconstruction by solving the sub-problem for \mathbf{f} . The regularization prior has an important effect on the final reconstruction. Among many priors for image reconstruction, including dictionary learning²⁰, low-rank²¹, sparsity²², and others²³, in this study we use a simple TV-type regularizer to emphasize the sparsity:

$$g(\mathbf{f}) = \sum_{i=2}^I \sum_{j=2}^J (|\mathbf{f}(i, j) - \mathbf{f}(i-1, j)| + |\mathbf{f}(i, j) - \mathbf{f}(i, j-1)|), \quad i=1, \dots, I; j=1, \dots, J,$$

where I and J represent the width and height of a reconstructed image, and the gradients on the image border are set to zero. Thus, $\mathbf{f}^{(k+1)}$ can be updated as follows:

$$\mathbf{f}^{(k+1)} = \arg \min_{\mathbf{h}} \left(\frac{1}{2} \|\mathbf{f} - \mathbf{f}^{(k)} - \mathbf{u}^{(k+1)}\|_F^2 + \eta \left(\sum_{i=2}^I \sum_{j=2}^J (|\mathbf{f}(i, j) - \mathbf{f}(i-1, j)| + |\mathbf{f}(i, j) - \mathbf{f}(i, j-1)|) \right) \right),$$

Replacing $\mathbf{f}(i, j) - \mathbf{f}(i-1, j)$ and $\mathbf{f}(i, j) - \mathbf{f}(i, j-1)$ with $\mathbf{d}_1(i, j)$ and $\mathbf{d}_2(i, j)$ respectively, we have the following unconstrained problem:

$$\left\{ \mathbf{f}^{(k+1)}, \mathbf{d}_1, \mathbf{d}_2 \right\} = \arg \min_{\{\mathbf{h}, \mathbf{d}_1, \mathbf{d}_2\}} \left(\frac{1}{2} \|\mathbf{f} - \mathbf{f}^{(k)} - \mathbf{u}^{(k+1)}\|_F^2 + \eta \left(\sum_{i=1}^I \sum_{j=1}^J (|\mathbf{d}_1(i, j)| + |\mathbf{d}_2(i, j)|) \right) + \rho \times \left(\sum_{i=1}^I \sum_{j=1}^J \left(\|\mathbf{d}_1(i, j) - (\mathbf{f}(i, j) - \mathbf{f}(i-1, j))\|_F^2 + \|\mathbf{d}_2(i, j) - (\mathbf{f}(i, j) - \mathbf{f}(i, j-1))\|_F^2 \right) \right) \right),$$

The above optimization problem can be solved by alternately minimizing the objective function. An FFT-based algorithm, named FTVD²⁴, is employed to find the solution. Note that there are two parameters in the above problem: η and ρ . These parameters are made the same in this study; i.e., $\eta = \rho = \delta$.

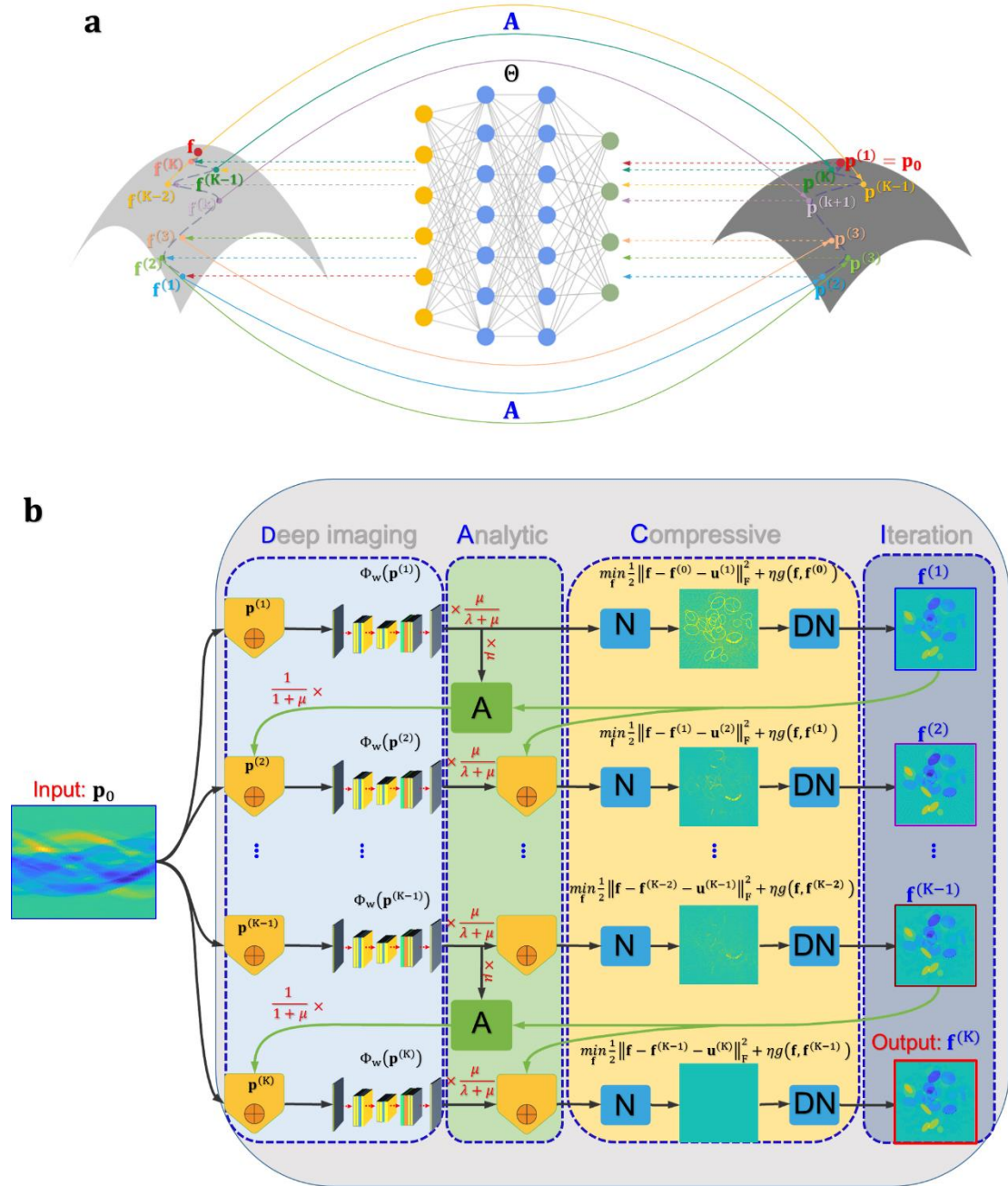


Figure 2 | ACID mechanism and architecture for stabilizing deep tomographic image reconstruction. **a**, The mechanism of the ACID approach. A continuous mapping of the residual between the original measurement and the estimation based on an intermediate image using a supervised/unsupervised transform Θ by minimizing $\|\mathbf{p} - (\mathbf{p}_0 - \mathbf{A}\mathbf{f})\|_F^2$. This process is interactively implemented for the optimal performance (for more details; see the Methods section), where the transform Θ performs deep learning and compressive sensing synergistically. **b**, The implementation details of the ACID reconstruction method. ACID consists of four components: analytic mapping, deep imaging, compressed sensing and iterative reconstruction, where “N” and “DN” denote normalization and de-normalization respectively.

Mechanism of ACID: As demonstrated in Fig. 2, the mechanism of ACID consists of four modules: error feedback adjustment, analytic mapping, deep learning, and compressed sensing. The idea of ACID is based on the error reduction iteration, which is a key component of a typical automatic control system. Specifically, the currently estimated measurement for image refinement at the $(k+1)^{\text{th}}$ iteration can be computed after obtaining the corresponding image $\mathbf{f}^{(k)}$ by passing it through the analytic operator \mathbf{A} by $\mathbf{p}^{(k+1)} = (\mu\mathbf{A}^{-1}\mathbf{u}^{(k)} + \mathbf{p}_0 - \mathbf{A}\mathbf{f}^{(k)}) / (1 + \mu)$.

Such an error feedback is essential to recover structural subtleties that can be lost in an open-loop feedforward information processing workflow. Since \mathbf{A} is an analytic operator, it can be efficiently executed. This analytic operation computes the residual data between the original tomographic data and the data estimated at the k^{th} iteration. This mechanism helps effectively suppress mismatches and/or inconsistencies caused by existing deep learning methods^{25,26}.

The output of the analytic mapping module is the input to the DL reconstruction network. The trained neural network performs image reconstruction to obtain an intermediate image. The function of the deep learning network at each iteration is to produce a gradually improved reconstruction $\Phi_w(\mathbf{p}^{(k+1)})$.

There are typically remaining artifacts or noise in the output of the DL network at each iteration. It is easy to understand that the DL network is trained on original images but it may not directly produce an output image that is consistent to the sparsity requirement by compressed sensing. This issue can be addressed by the CS module, which can be implemented in terms of total variation²⁷, low-rank²⁸, dictionary learning²⁹, etc. In this study, the anisotropic TV is employed to enforce sparsity at each iteration³⁰. Note that the generic TV favors piecewise constant regions, while high-order TV encourages piecewise polynomials³¹. Here, the input to the CS module is normalized to $[0, 1]$ to facilitate the selection of the regularized parameters, which requires de-normalization of the output of the CS module.

III. Results

Data Preparation & Network Training: The EIL-50 and DAGAN networks were employed to validate the effective of our proposed ACID in both CT and MRI cases respectively. First, with the EIL-50 network for CT, the projection data were generated using the *radon* and *iradon* functions in MATLAB R2017b, where 50 means the number of projection views. To ensure the fidelity of this experiment, we just used the trained networks in³², which are the same as that used in the experiments³³. The test data for Case C1 was provided by the authors of³³, which can be download freely from the website³⁴. Cases C2 and C3 with the logo of bird embedded were provided by the authors of¹⁴ and downloaded from the website³⁵. The test images consists of 512×512 pixels and contain structural changes without tiny perturbation. To further generate adversarial attacks, the proposed method in³³ was employed to induce tiny perturbations. Then, we obtained C4-C6 by adding tiny perturbations to C1-C3 respectively. For the EIL-50 network, it was implemented on Matlab 2017b with the MatConvNet platform based on the Window 10 system, with one NVIDIA TITAN XP graphics processing units (GPUs) stalled on a PC (16 CPUs @3.70GHz, 32.0GB RAM and 8.0GB VRAM).

For evaluation of ACID in MRI, the DAGAN method was employed³⁶, which was proposed for

single coil MRI reconstruction. The sub-sampling rates in DAGAN can be freely selected. In this study, we set the subsampling rate to 10% and subsampled these images with the 2D Gaussian sampling pattern. Also, we re-trained the DAGAN network, where the number of epoch was set to 50 with the other parameters and the training datasets being the same as what were previous used³⁶. The test images are a series of brain images, each of which consists of 256×256 pixels. Case M1 was randomly chosen from the test data³⁶, then the symbol “HELLO NATURE” was introduced into the image as structural changes. Case M2 is the same as that given in³³, where the symbol “CAN U SEE IT” and “◇” were added to the original image. Furthermore, the uniform noise with zero mean and 15 deviation over the image pixel value range [0 255] was added to Cases M1 and M2 to obtain Cases M3 and M4. Also, we adopted the same technique used by the authors of³³ to generate adversarial attacks. The resultant tiny perturbations were added to Cases M1-M2 to obtain Cases M5-M6³³. For training and testing the DAGAN network, it was implemented on TensorFlow 1.8.0 based on the Windows 10 system configured with GPU-1080ti on a PC (28 CPUs @2GHz, 64GB RAM).

Performance Valuation & Comparison: To quantitatively compare the results of different reconstruction methods, the root mean square error (RMSE) and the peak signal-to-noise ratio (PSNR) were employed to measure the difference between reconstructed images and the ground truth. More relevantly, the structural similarity (SSIM) was also used to assess the similarity between reconstructed images and the ground truth. For qualitative analysis, visual inspection of structural changes (i.e., the insert text, bird, and patterns) and artifacts induced by tiny perturbation was performed to evaluate reconstructed results. In this context, we mainly focused on assessing features details such as image edges and structural integrity.

To demonstrate the superior performance of ACID and highlight its stability against noise and attack, the state-of-art CS based methods were chosen as the reference. Specifically, for CT, the sparse regularization based CS method combining X-lets (shearlets) and TV was selected as the CS benchmark³⁷, which is consistent with the selection in³³. For MRI, the total generalized variation (TGV) method was chosen as the CS benchmark³⁸. All the parameters including the number of iterations for these CS methods were optimized for fair comparison of quantitative and qualitative results.

Stability with Small Structural Changes: We first demonstrate the robust performance of the ACID network with small structural changes. Fig. 3 shows representative results in 3 cases, i.e., C1-C3. To examine the degrees of small image structure recovery allowed by all reconstruction methods, some texts, a bird, and their mixture were used to simulate the structural changes to CT images. It can be observed in Fig. 3 that the proposed ACID strategy provided a superior performance thanks to the synergistic fusion of analytic solution, compressed sensing, refinement iteration, and deep learning. In this case, the EII-50 served as the deep network for data-driven image estimation. It can be clearly observed in Fig. 3 that CS reconstructions can give better results than the EII-50 network. It is consistent to the results reported in the PNAS paper³³. Because the CS based methods perform conventional unsupervised, model-based and sparsified reconstruction, structural changes are within the sparsity constraint and cannot be lost in the reconstruction. Specifically, we cannot see the texts and bird in the EII-50 reconstruction at all. The text “CAN U SEE IT” and the bird were damaged by the artifacts in the CS reconstruction. The compromised versions of the text and the bird are

still identifiable with the CS method, despite the poor image quality. As expected, the symbol “CAN U SEE IT” and the bird can be well recovered using our ACID network. The bird in C2 and C3 cannot be resolved at all using the EII-50 network. The contour of the bird can be identified in the CS reconstructions among the artifacts due to the under-sampled data ³⁹. In terms of image edge preservation, the EII-50 reconstruction contains clearer edges than those in the CS reconstruction. Compared to the basic EII-50 prediction, ACID can correct structural distortion by avoiding the projection distortion via iterative refinement. This point is evidenced by the structure indicated by the white arrow in Fig. 3. ACID exhibits the superior stability with structural changes over the CS and EII-50 methods, as quantified by the three metrics including the root-mean-squared error (RMSE), peak image signal-to-noise ratio (PSNR), and structural similarity (SSIM) (Fig. 3). In all these results, the ACID always obtains the smallest RMSE, the greatest PSNR, and the highest SSIM. It is remarkable that the RMSE can be decreased by ACID to one-third to one-half of that associated with the CS and EII-50. Besides, the SSIM values can also significantly improved by ACID, which means that the ACID has a great potential to meet the requirement of challenging practical applications.

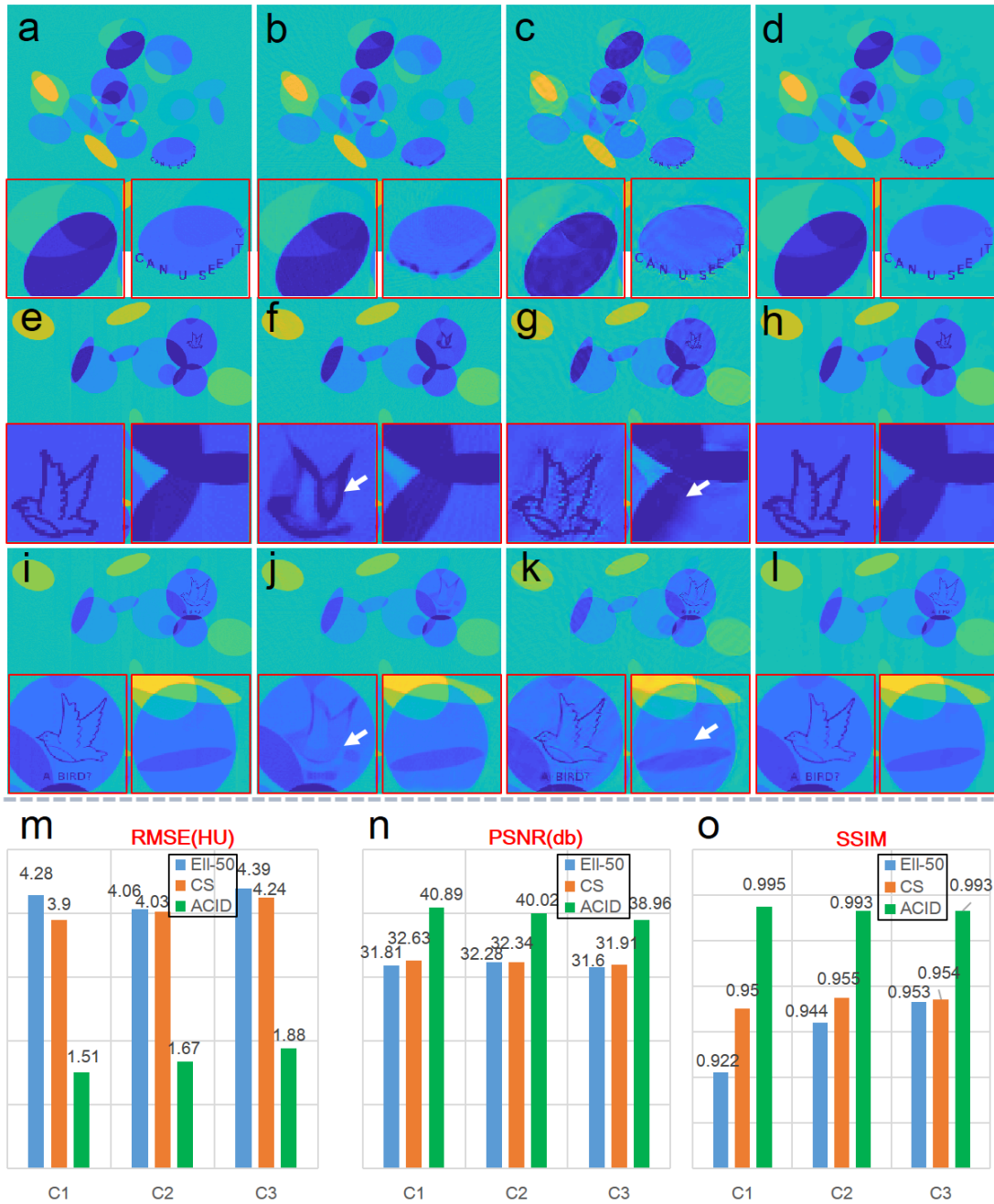


Figure 3 | Performance of ACID with small structural changes in the CT case. Three different phantoms with structural changes were reconstructed by both ACID and conventional techniques; **a**, **e** and **i** represent the original images. **b**, **f** and **g** are the results reconstructed with EII-50; **c**, **g** and **k** represent the corresponding CS results; **d**, **h** and **i** represent the ACID results. Quantitative results in terms of RMSEs, PSNRs and SSIMs of C1-C3 for all competing methods are in **m–o**. The windows of Cases C1-C3 are [-150 150], [-150 150] and [-200 200] respectively.

After testing ACID with CT data, we further performed a similar study on ACID in the MRI case with small structural changes, as shown in Fig. 4. As mentioned earlier, DAGAN was implemented for comparison. In this case, the symbol “HELLO NATURE” was added to one brain MRI slice. Fig. 4 b-d are the results reconstructed from data subsampled at a rate 10%.

It can be seen that structures of "HELLO NATURE" were severely corrupted by DAGAN, which makes it difficult to recognize these structures. The structures were effectively recovered by the CS method but there are still strong artifacts induced by the low subsampling rate. In addition, the image edges of "HELLO NATURE" are too blurry to be easily visible. On the other hand, our ACID network produced crystal clear results.

To further show the power of ACID with small structural changes, another example given in ³³ was also reproduced as Fig. 4f-h using the competing reconstruction techniques. The text "CAN U SEE IT" was corrupted by both DAGAN and CS, rendering the insert challenging to be read. Again, it can be easily seen in the reconstruction by ACID. Indeed, compared with the DAGAN and CS results, the ACID reconstruction keeps sharp image edges and subtle features of the text "CAN U SEE IT". The reconstructed results from M2 (similar to the DAGAN results in ³³ but with a different subsampling rate and sampling pattern) further confirm the superior performance of ACID. The reconstruction results from M3-M4 generated by adding random noise to M1-M2 are also given in Fig. 4. In this situation, both DAGAN and CS results were corrupted by noise, with the image edges and other features further blurred, especially for the CS results. Compared with the CS results, DAGAN seems providing clearer image edges and shapes while the text such as "HELLO NATURE" was still quite blurred. In contrast, these words were nicely recovered by ACID. To further validate these exciting results, the quantitative results on this MRI experiment are reported in Fig. 4 q-s. Indicated by these quantitative results, ACID produced the smallest RMSE, the greatest PSNR, and the highest SSIM. Again, the RMSE was decreased by ACID to one-third to one-half of that associated with the CS and EII-50. Also, the SSIM and PSNR values was significantly improved by ACID. It can be seen in Fig. 4 q-s that image noise reduced the performance of all reconstruction methods, but ACID remained the best among all the compared methods.

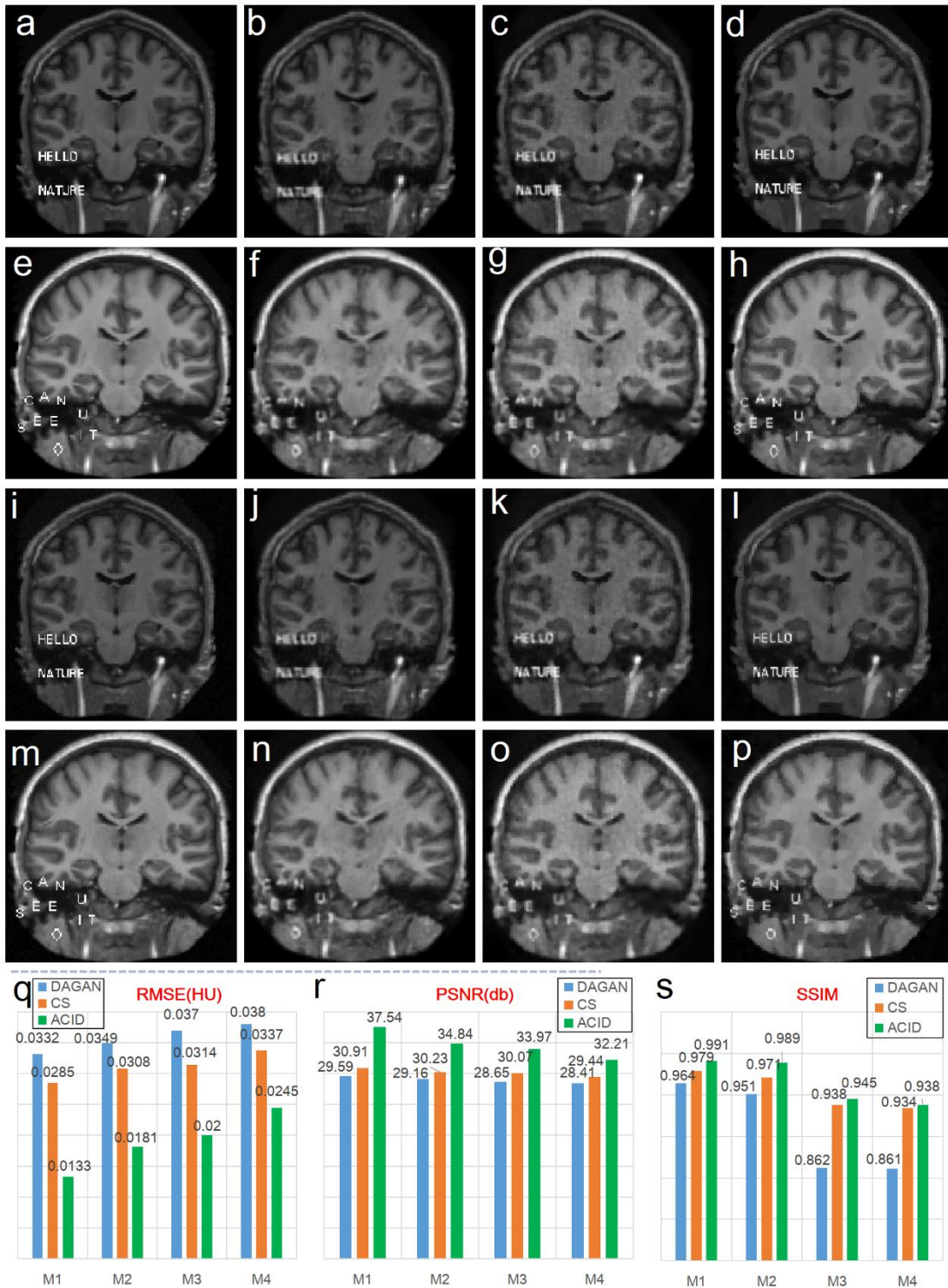


Figure 4 | Performance of ACID with small structural changes in the MRI case. a–d, e–h, i–l and m–p represent the original images, the images reconstructed by DAGAN, CS and ACID from M2-M4 respectively. The images were reconstructed from data by subsampling the original images with a 2D Gaussian sampling pattern and a subsampling rate 10%. The images were normalized to [0 1].

Stability against Tiny Perturbation: It was pointed out that a tiny perturbation could fool a deep neural network to make a highly undesirable prediction³³. To show the capability of the ACID approach against tiny perturbations, the CT and MRI reconstruction results are given in Fig. 5. From the C4 results in Fig. 5a₂-a₄, the edges obtained using EII-50 indicated by the arrows were distorted by perturbation. Although the CS reconstruction had a stable performance against tiny perturbations, these distortions cannot be fully corrected in the corresponding results due to the subsampling artefacts. However, this defect was well fixed by ACID. It is easy to understand that our ACID works stably aided by both the error correction and CS modules. The synergistic nature of the ACID components makes it powerful in correcting distortions and artifacts while suppressing image noise as well. Regarding the results in Fig. 5b₂-b₄, it is observed that the artifacts marked by the arrows induced by perturbation could be viewed as tumors in the EII-50 reconstruction. This would result in a wrong clinical decision in practice. Although such artefacts were eliminated in the CS reconstruction, the artifacts from subsampling were clearly introduced. In contrast, the corresponding edges and shapes were clearly reproduced by ACID without any significant artefacts. Regarding the results of C3 in Fig. 5C₂-C₄, the bird features and the text "BIRD?" were totally lost in the EII-50 reconstruction, severe artifacts were induced by the CS method. In contrast, our ACID results are of high quality faithful edges and letters.

As far as our MRI results are concerned, the worst predictions from tiny perturbations are obvious in Fig. 5d₂ and e₂. Based on the DAGAN results, we see that DAGAN would fail upon adversarial attacking. Tiny perturbations could result in wrong structures and details, as shown in Fig. 5d₂ and e₂. In other words, it is dangerous using this class of neural networks in applications. Compared with DAGAN results, the CS reconstruction provided higher accuracy. However, the CS method failed to preserve details such as edges in subsampling cases, which are shown in Fig. 4d₃ and e₃. Remarkably, our ACID network is free from these weaknesses. To further highlight the superiority of ACID, the quantitative results are included in Fig. 6.

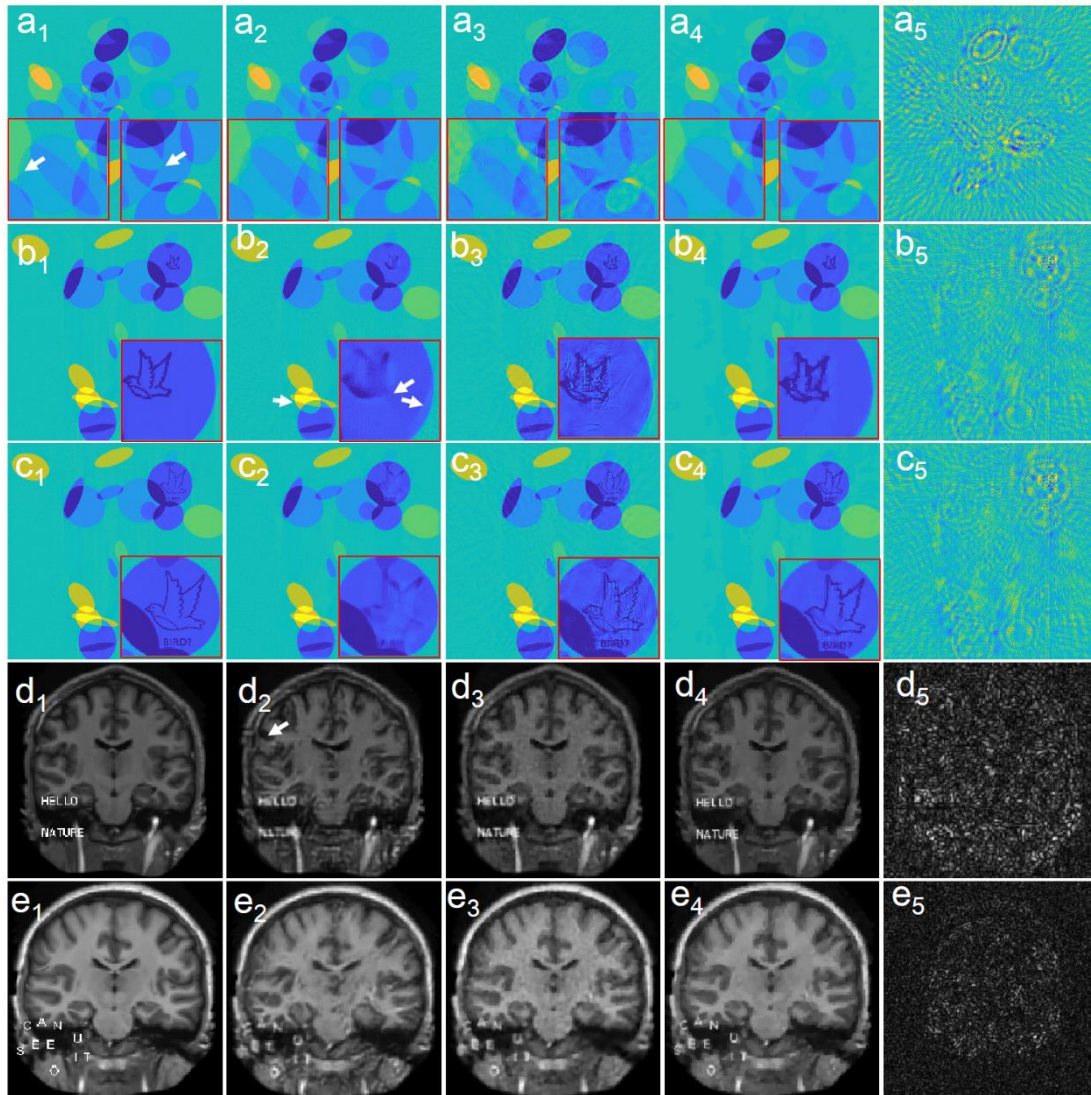


Figure 5 | Performance of ACID with tiny perturbation and structural changes simultaneously in the MRI and CT cases. a_1 , b_1 , c_1 , d_1 and e_1 are the images after adding tiny perturbations to the original images. a_2 - a_4 , b_2 - b_4 , c_2 - c_4 , d_2 - d_4 and e_2 - e_4 represent the reconstructed images in the **C1**, **C2**, **C3**, **M1** and **M2** cases using DAGAN, CS and ACID respectively. a_5 , b_5 , c_5 , d_5 and e_5 are the perturbations to the original images. The display windows are the same as that used for Figs. 3 and 4.

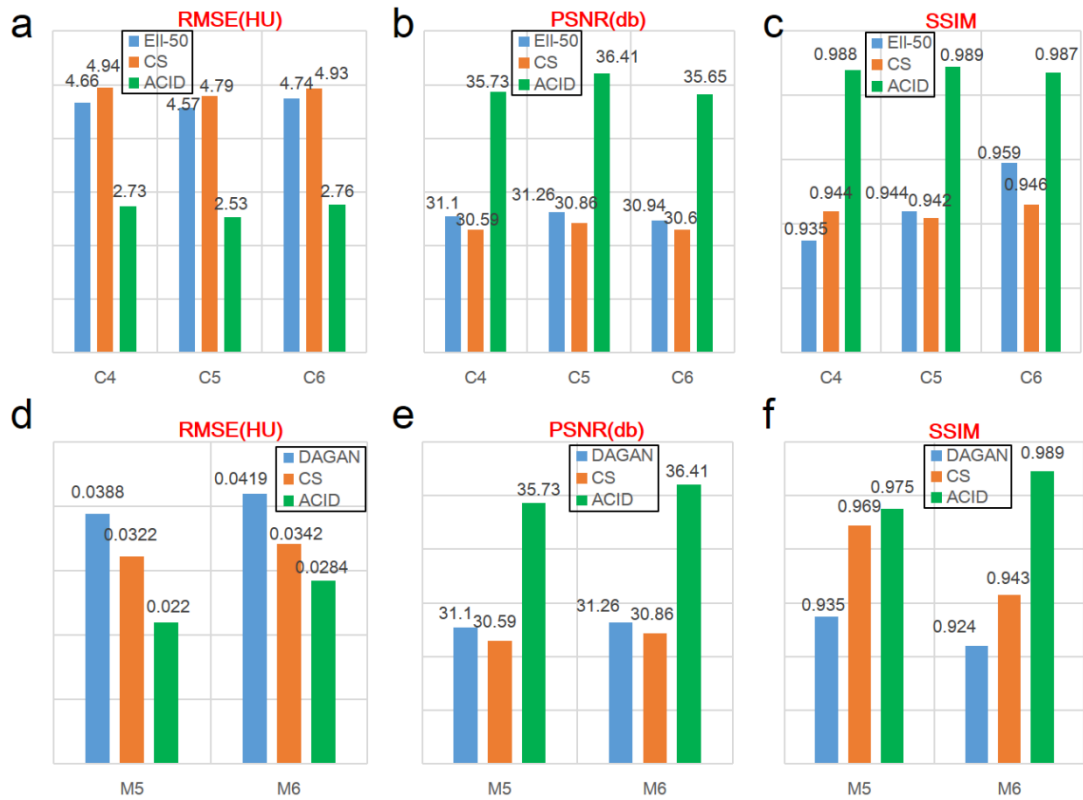


Figure 6 | Quantification of the ACID results in Fig. 5, in terms of RMSE, SSIM and PSNR. a-c represent the RMSE, SSIM and PSNR results on C4-C6. d-f represent the RMSE, SSIM and PSNR results on M5-M6.

Stability for More Input Data: The performance of ACID will monotonically increase as more input data become available, which is certainly expected of a well-designed network. With EII-50 and DAGAN as examples, it was pointed out by the authors of ³³ that the performance of deep reconstruction networks could be degraded with more input data, which is counter-intuitive and highly undesirable. To evaluate the performance of our ACID network in this regard, the results from Cases C1, M1 and M2 were analyzed. Our key results are shown in Fig. 7, where the number of views in the CT scenario were chosen as 10, 20, 30, 40, 50, 60, 75, 100, 150 and 300 respectively, while in the MRI scenario the subsampling rate was set to 1%, 5%, 10%, 20%, 30%, 40% and 50% respectively. It is observed in Fig. 7a-c, that the performances of EII-50 would be compromised with more views, being consistent with what was reported in ³³, but the performance of ACID performed better with larger number of views in terms of RMSE, PSNR and SSIM respectively. Similarly Fig. 7d-l show that the performance of DAGAN would be decreased at subsampling rates larger than that used for training DAGAN, which is the same conclusion made on DAGAN in ³³, and ACID produced better results in terms of RMSE, PSNR and SSIM respectively.

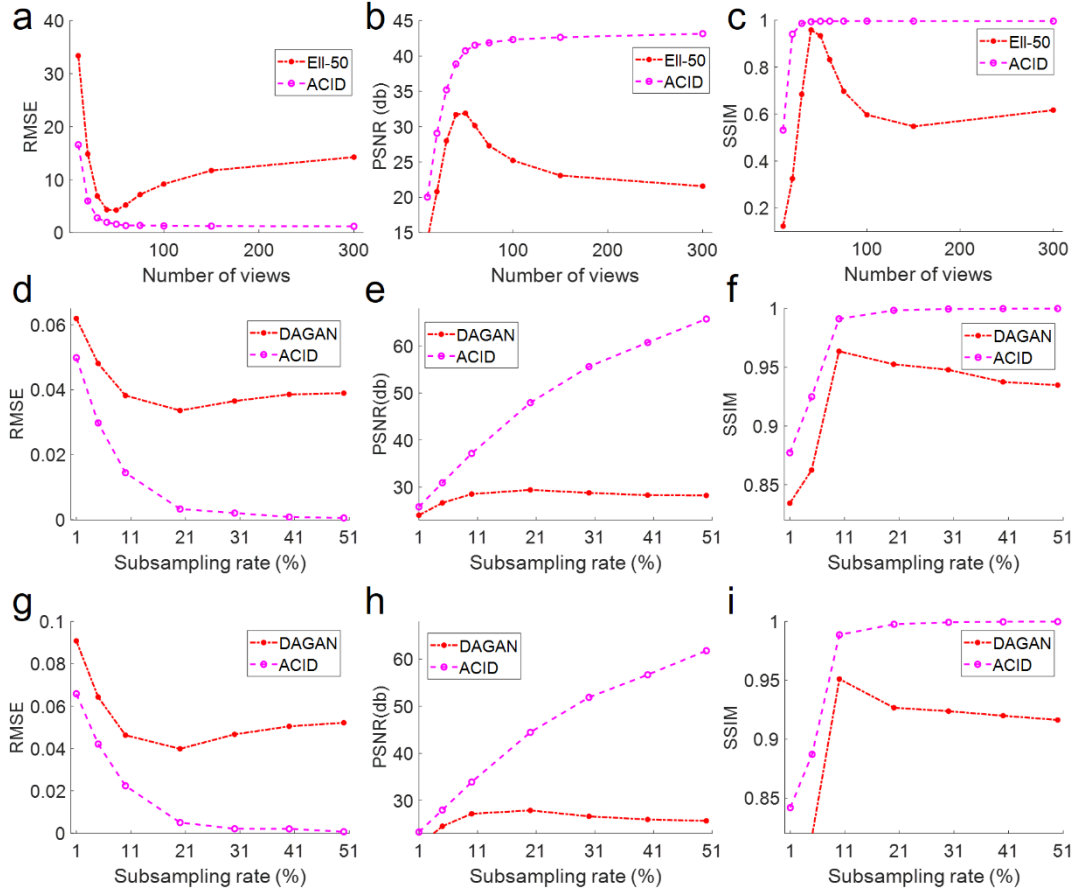


Figure 7 | Stability Quantification of ACID in Cases of C1, M1 and M2 with more input data. **a-c** represent the RMSE, PSNR and SSIM curves on C1 with respect to the number of views. **d-f** and **g-i** represent the RMSE, PSNR and SSIM results from M1 and M2 with respect to the subsampling rate.

ACID Parameterization: The proposed ACID method mainly use three parameters: λ , μ and δ . The ACID reconstruction model focuses on characterizing the residual error between real and estimated measurements. Although the ACID model may appear somehow similar to the CS based reconstruction model, the selection of parameters λ and μ are different from what is typically done for the CS reconstruction. Specifically, the parameters of ACID are optimized by comparing quantitative and qualitative results numerically and/or experimentally, as listed in Table I. It can be seen that all parameters are relatively small.

Table I. Parameters used in experiments.

CT	C1	C2	C3	C4	C5	C6
$\delta(10^{-3})$	1.50	1.20	1.75	1.10	0.8	0.8
$\mu(10^{-3})$	150	130	220	0.10	0.1	5.0
$\lambda(10^{-2})$	15.0	8.00	2.0	0.03	0.03	1.2
MR	M1	M2	M3	M4	M5	M6
$\delta(10^{-3})$	0.40	0.334	0.50	0.40	0.67	0.50
$\mu(10^{-3})$	31.0	32.0	31.0	30.0	29.0	30.0
$\lambda(10^{-2})$	1.00	0.80	1.0	0.80	1.10	1.00

Convergence Analysis & Computational Cost: We assessed the reconstruction convergence and computational cost, since the ACID network is sophisticated; for example, it demands the residual projections through an intermediate image. Because it is overwhelming to theoretically analyze the convergence of ACID, in this study we experimentally tested the convergence of ACID. We used RMSE as the metric to probe the convergence of ACID, as shown in Fig.8. It can be seen that ACID can converge after about 30 iterations for CT, and it becomes stable after 250 iterations for MRI. Therefore, in this study we set the number of iteration to 50 and 300 for CT and MRI respectively.

In a good sense, ACID is iterative. Hence, we need to balance the imaging performance and the computational cost. In fact, our method can still satisfy the requirement of fast imaging. First, we just use analytic forward projection and back-projection operators that can be done rapidly, instead of more elaborative steps in a modern iteration for image reconstruction. Also, we implemented the CS module based on a TV-type regularizer using a FFT-based method, which can also be performed very fast. For example, 50 iterations for ACID for CT based on the EIL-50 network takes less than 35 seconds.

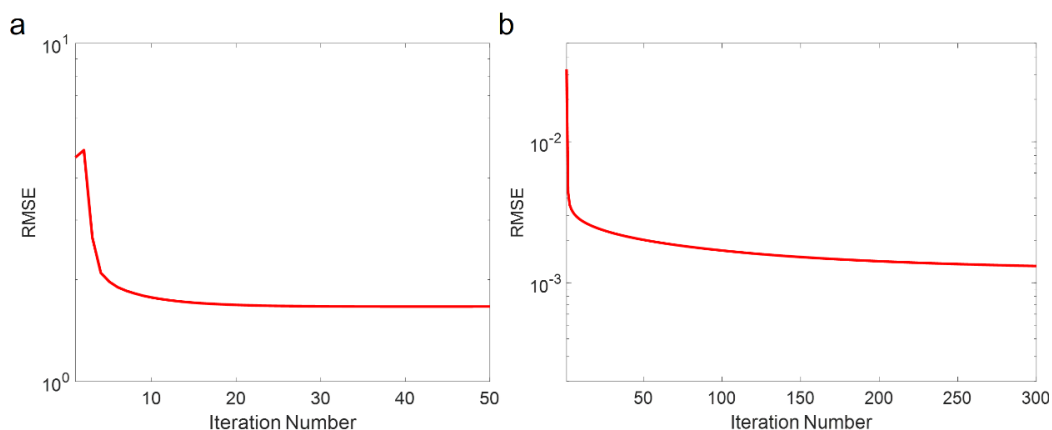


Figure 8 | Convergence of ACID in terms of RMSE in the C2 and M2 cases. a and b show the convergence curves of C2 and M2 respectively.

IV. Discussions & Conclusion

The aforementioned “*kernel awareness*”¹⁴ is to avoid the so-called “*cardinal sin*”, which means to recovering elements close to the null space of an imaging operator A . In other words, suppose that two images x and x' correspond to datasets Ax and Ax' respectively, if the two datasets are very close to each other while the two images significantly differ and yet these images are accurately reconstructed using a continuous algorithm, then the algorithm will be intrinsically unstable, suffering from false positives and false negatives; for mathematical rigor, please see Theorem 3.1 in¹⁴. To a major degree, the deep tomographic networks were successfully attacked in⁶. On the other hand, compressed sensing reconstruction algorithms were designed with the kernel awareness, leading to accurate and stable recovery of underlying images, as also shown in⁶. As demonstrated by our work, the kernel awareness is embedded in the ACID network so that it shows robust performance against noise, under adversarial attacks, and when input data are increased relative to what is assumed in the network training.

It is important to understand how a compressed sensing algorithm implements the kernel

awareness. Basically, the compressed sensing solution to the inverse problem is obtained under the sparsity constraint so that the search for the solution is strongly constrained within a low-dimensional manifold (the solution must be sparse in a proper sense). That is, prior knowledge known as sparsity helps effectively regularize the solution space. Indeed, natural and medical images allow low-dimensional manifold models⁴⁰. It is critically important to underline that a deep neural network is data-driven, and the resultant data-driven priors are rather powerful to constrain the solution space for tomographic imaging, if the network is appropriately design. While priors for compressed sensing are just one or a few mathematical expressions, deep priors are in a network format and extracted from big data. These two kinds of priors are actually combined in our ACID network to have the merits from both sides, and we have fundamental reasons to expect that ACID or similar networks would output classic algorithms including CS methods.

In conclusion, our ACID network synergizes key elements of analytic, compressed sensing, iterative reconstruction, and deep learning, have systematically fixed instabilities of the deep reconstruction networks selected in⁶ and consistently produced better results than the state of the art compressed sensing algorithm used in the same study. It is emphasized that our ACID network is only an embodiment, and other advanced deep reconstruction networks are certainly needed for different tasks in the same spirit of being aware of data, kernel, efficiency, and other factors. We believe that attack and defense is just like the arms race, in which deep reconstruction networks will be further developed and become standard tools in the medical imaging arsenal.

References

- 1 Fuchs, V. R. & Sox Jr, H. C. Physicians' views of the relative importance of thirty medical innovations. *Health Affairs* **20**, 30-42 (2001).
- 2 Wang, G. A Perspective on Deep Imaging. *IEEE Access* **4**, 8914-8924, doi:10.1109/Access.2016.2624938 (2016).
- 3 Wang, G., Ye, J. C., Mueller, K. & Fessler, J. A. Image Reconstruction is a New Frontier of Machine Learning. *IEEE Trans Med Imaging* **37**, 1289-1296, doi:10.1109/TMI.2018.2833635 (2018).
- 4 Wang, G., Zhang, Y., Ye, X. J. & Mou, X. Q. *Machine learning for tomographic imaging.* (IOP Publishing, 2019).
- 5 Wang, G., Ye, J. C. & De Man, B. *Deep Learning for Tomographic Imaging.* *Nature Machine Intelligence*, revision pending review (2020).
- 6 Antun, V., Renna, F., Poon, C., Adcock, B. & Hansen, A. C. On instabilities of deep learning in image reconstruction and the potential costs of AI. *Proceedings of the National Academy of Sciences of the United States of America*, doi:10.1073/pnas.1907377117 (2020).
- 7 Zhu, B., Liu, J. Z., Cauley, S. F., Rosen, B. R. & Rosen, M. S. Image reconstruction by domain-transform manifold learning. *Nature* **555**, 487-492 (2018).
- 8 Natterer, F. *The mathematics of computerized tomography.* (SIAM, 2001).
- 9 Kak, A. C., Slaney, M. & IEEE Engineering in Medicine and Biology Society. *Principles of computerized tomographic imaging.* (IEEE Press, 1988).
- 10 Vogel, R. A., Kirch, D., LeFree, M. & Steele, P. A new method of multiplanar emission tomography using a seven pinhole collimator and an Anger scintillation camera. *J Nucl Med* **19**, 648-654 (1978).
- 11 Nuyts, J., De Man, B., Fessler, J. A., Zbijewski, W. & Beekman, F. J. Modelling the physics in the iterative reconstruction for transmission computed tomography. *Physics in medicine and biology* **58**, R63 (2013).
- 12 Candes, E. J. & Tao, T. Near-optimal signal recovery from random projections: Universal encoding strategies? *IEEE transactions on information theory* **52**, 5406-5425 (2006).
- 13 Herman, G. T. & Davidi, R. Image reconstruction from a small number of projections. *Inverse problems* **24**, 045011 (2008).
- 14 Gottschling, N. M., Antun, V., Adcock, B. & Hansen, A. C. The troublesome kernel: why deep learning for inverse problems is typically unstable. *arXiv preprint arXiv:2001.01258* (2020).
- 15 Wang, G. Tomographic Reconstruction with Machine Learning, <<https://www.nibib.nih.gov/news-events/meetings-events/artificial-intelligence-medical-imaging-workshop>> (2018).
- 16 Wang, G. Tomography With Deep Learning, <<https://math.tufts.edu/faculty/equinto/Cormack2019/TalkSlides/GeWang.pdf>> (2019).
- 17 Katsevich, A. Analysis of an exact inversion algorithm for spiral cone-beam CT. *Physics in Medicine and Biology* **47**, 2583 (2002).
- 18 Axel, L., Summers, R., Kressel, H. & Charles, C. Respiratory effects in two-dimensional Fourier transform MR imaging. *Radiology* **160**, 795-801 (1986).

- 19 Viswanathan, J. & Grossmann, I. E. A combined penalty function and outer-approximation method for MINLP optimization. *Computers and Chemical Engineering* **14**, 769-782 (1990).
- 20 Ravishankar, S. & Bresler, Y. MR image reconstruction from highly undersampled k-space data by dictionary learning. *IEEE transactions on medical imaging* **30**, 1028-1041 (2010).
- 21 He, J. et al. Accelerated high-dimensional MR imaging with sparse sampling using low-rank tensors. *IEEE transactions on medical imaging* **35**, 2119-2129 (2016).
- 22 Vasanawala, S. S. et al. Improved pediatric MR imaging with compressed sensing. *Radiology* **256**, 607-616 (2010).
- 23 Chan, R. H., Chan, T. F., Shen, L. & Shen, Z. Wavelet algorithms for high-resolution image reconstruction. *SIAM Journal on Scientific Computing* **24**, 1408-1432 (2003).
- 24 Wang, Y., Yin, W. & Zhang, Y. A fast algorithm for image deblurring with total variation regularization. (2007).
- 25 Wu, D., Kim, K., El Fakhri, G. & Li, Q. Iterative low-dose CT reconstruction with priors trained by artificial neural network. *IEEE transactions on medical imaging* **36**, 2479-2486 (2017).
- 26 Shen, C., Gonzalez, Y., Chen, L., Jiang, S. B. & Jia, X. Intelligent parameter tuning in optimization-based iterative CT reconstruction via deep reinforcement learning. *IEEE transactions on medical imaging* **37**, 1430-1439 (2018).
- 27 Rudin, L. I., Osher, S. & Fatemi, E. Nonlinear total variation based noise removal algorithms. *Physica D: nonlinear phenomena* **60**, 259-268 (1992).
- 28 Liu, G. et al. Robust recovery of subspace structures by low-rank representation. *IEEE transactions on pattern analysis and machine intelligence* **35**, 171-184 (2012).
- 29 Tomic, I. & Frossard, P. Dictionary learning. *IEEE Signal Processing Magazine* **28**, 27-38 (2011).
- 30 Chen, Z., Jin, X., Li, L. & Wang, G. A limited-angle CT reconstruction method based on anisotropic TV minimization. *Physics in Medicine and Biology* **58**, 2119 (2013).
- 31 Wang, Y., Yang, J., Yin, W. & Zhang, Y. A new alternating minimization algorithm for total variation image reconstruction. *SIAM Journal on Imaging Sciences* **1**, 248-272 (2008).
- 32 Jin, K. H., McCann, M. T., Froustey, E. & Unser, M. Deep convolutional neural network for inverse problems in imaging. *IEEE Transactions on Image Processing* **26**, 4509-4522 (2017).
- 33 Antun, V., Renna, F., Poon, C., Adcock, B. & Hansen, A. C. On instabilities of deep learning in image reconstruction and the potential costs of AI. *Proceedings of the National Academy of Sciences* (2020).
- 34 Antuna, V., Rennab, F., Poonc, C., Adcockd, B. & Hansen, A. C. <https://github.com/vegarant/Invfool>, 2020).
- 35 M, N., Gottschling, Antun, V., Adcock, B. & Hansen, A. C. https://github.com/vegarant/troub_ker, 2020).
- 36 Yang, G. et al. DAGAN: Deep de-aliasing generative adversarial networks for fast compressed sensing MRI reconstruction. *IEEE transactions on medical imaging* **37**, 1310-1321 (2018).

- 37 Ma, J. & März, M. A multilevel based reweighting algorithm with joint regularizers for sparse recovery. *arXiv preprint arXiv:1606.06941* (2016).
- 38 Knoll, F., Clason, C., Bredies, K., Uecker, M. & Stollberger, R. Parallel imaging with nonlinear reconstruction using variational penalties. *Magnetic resonance in medicine* **67**, 34-41 (2012).
- 39 Yu, H. & Wang, G. Compressed sensing based interior tomography. *Physics in medicine and biology* **54**, 2791 (2009).
- 40 Cong, W. et al. CT image reconstruction on a low dimensional manifold. *Inverse Problems and Imaging* **13** (2019).